JOURNAL OF AIRCRAFT
Vol. 39, No. 6, November–December 2002

Effects of Surface Ice Roughness on Dynamic Stall

Wade W. Huebsch*
West Virginia University, Morgantown, West Virginia 26506-6106
and
Alric P. Rothmayer†
Iowa State University, Ames, Iowa 50011-2271

A two-dimensional Navier–Stokes algorithm is used to investigate unsteady, incompressible viscous flow past an airfoil leading edge with surface roughness that is characteristic of early-growth ice accretion. The roughness is added to the surface through the use of a Prandtl transposition and can generate both small-scale and large-scale roughness geometries. The algorithm is used to simulate steady or unsteady flow at constant angle of attack or pitch up corresponding to dynamic-stall conditions. Investigations of the dynamic stall show that some types of surface roughness can significantly alter the unsteady flow separation pattern and the formation of the dynamic-stall vortex. This includes both small-scale and large-scale roughness.

Nomenclature

c = airfoil chord length
$f(\xi)$ = analytic expression for roughness geometry
h = hump height
$K(t)$ = angle-of-attack parameter
l = leading-edge radius of curvature for parabola
Re = Reynolds number
$\dot{\alpha}$ = pitch rate
β = scale factor for governing equations
$\eta', \eta, \bar{\eta}$ = normal coordinates
$\xi', \xi, \bar{\xi}$ = streamwise coordinates
τ = pseudotime
ψ, Ψ = stream function
ω, Ω = vorticity

Subscripts

inv = inviscid value
L, R = left and right locations, respectively
w = value at the wall
∞ = freestream value

Introduction

IT is well known that airfoil leading edges can have a significant effect on the aerodynamic performance of the overall wing. For example, the NACA 23012 is a "front-loaded" airfoil, with a large suction peak located near the leading edge. If something hinders the formation of the leading-edge suction peak (such as in-flight ice accretion), the overall lift coefficient C_L can be severely degraded. In addition, the leading edge of an airfoil can significantly effect off-design performance due to the sensitive dependence of the flow about the leading edge to changes in geometry and flow conditions. For example, catastrophic failures, including failures caused by excessive aerodynamic loading, can occur through static and dynamic leading-edge stall. It has been documented by Potapczuk et al.,[1] Cebeci,[2] and Cebeci and Besnard[3] that leading-edge surface roughness, in particular ice roughness, can adversely effect the aerodynamic characteristics of a wing. The present work investigates the steady and unsteady flow about an airfoil leading edge, at constant angle of attack or in pitch up, with some surface protuberance that is characteristic of airfoil surface roughness or surface ice geometries. The pitch-up scenario in this study is used to simulate the dynamic stall in the leading-edge region.

Dynamic stall is a term used to describe the complex flow phenomenon on an airfoil (or wing) that is induced by pitching up rapidly from zero to a high angle of attack that is larger than the static-stall angle for the airfoil. The resulting flowfield for an airfoil that experiences a rapid unsteady pitch up is quite different than an airfoil in a quasi-steady-state motion. Shih et al.[4] noted that this difference is primarily due to the interaction of local unsteady boundary-layer separation and the external flow, which eventually leads to massive boundary-layer separation and the formation of large-scale vortices. This type of dominant vortex is referred to as a dynamic-stall vortex. Extensive reviews of experimental, analytical, and numerical studies of dynamic stall are given by Carr[5] and Carr and McCroskey.[6] There is also extensive literature available dealing with the actual process of dynamic stall.[4,5,7]

The dynamic stall analysis in this study is restricted to two-dimensional flow in the airfoil leading-edge region. It was shown by Robinson et al.[8] and Carr[5] that the flow away from the wing tip is nearly two-dimensional for a wing in pitch up. Shih et al.[4] show that the unsteady separation that leads to the formation of the dynamic-stall vortex is a local flow phenomena restricted to the leading-edge region and that the trailing-edge flow does not have a direct impact on the leading-edge separation process. Therefore, realistic and useful data can be obtained from this type of analysis. Note that in terms of the definition of dynamic stall,[7] the present study investigates the stages before full dynamic stall, that is, up to and including the formation of the vortex and vortex shedding in the leading-edge region.

Restricting the flow analysis to the leading edge of an airfoil (or wing) is prompted by the following reasons: 1) The most common surface roughness and the most significant ice accretion occur in this location. 2) This region is susceptible to many important flow phenomena, including leading-edge stall, thin airfoil stall, and dynamic stall. 3) The region close to the leading edge tends to remain laminar and at a low local Reynolds number, which simplifies the direct simulations. 4) Focusing on the leading-edge region significantly reduces the computational expense. This produces a solver that is clean and robust with no requirement for explicit artificial dissipation or other dissipation-inducing numerical devices. In addition, solving the unsteady flowfield only in the leading-edge region

---

Received 31 March 2002; revision received 27 June 2002; accepted for publication 2 July 2002.

*Assistant Professor, Department of Mechanical and Aerospace Engineering, P.O. Box 6106; Wade.Huebsch@mail.wvu.edu. Member AIAA.

†Professor, Department of Aerospace Engineering and Engineering Mechanics, 2271 Howe Hall. Member AIAA.

allows the use of a large number of grid points in the area of interest. In the current study, a dense grid is placed in the leading-edge region, which is capable of capturing small eddies within the boundary layer.

The present work focuses on steady and unsteady flow phenomena about the leading edge of an airfoil with surface roughness. Currently, most available data[4,5,9] for dynamic stall use smooth surfaces. Therefore, a need exists to examine the effects of surface roughness on dynamic stall. The objective of this study is to gain a better understanding of the interaction between leading-edge surface roughness and the formation of the dynamic-stall vortex. An algorithm has been developed to study the effects of surface roughness on leading-edge flow separation, unsteady vortex shedding, and local stall characteristics. The flowfield is modeled using the full unsteady, two-dimensional, incompressible Navier–Stokes equations. Roughness geometries are added to the surface using a Prandtl transposition, which allows for rapid analysis of different roughness geometries without the need to regrid. The algorithm has the capability of analyzing both steady flow at a constant angle of attack and unsteady flow at either constant angle of attack or in pitch up, which can lead to static and dynamic stall. Several different types of surface roughness are investigated including simple and complex hump roughness and simulated ice roughness.

Governing Equations

This section outlines the governing equations used for the flow calculations, as well as the corresponding boundary and initial conditions. The flow is modeled by the full Navier–Stokes equations for two-dimensional, unsteady, incompressible flow. The x and y coordinates are nondimensionalized by the leading-edge radius of curvature l, the u and v velocities by the freestream velocity V_∞, and the time t by l/V_∞. The resulting dimensionless Navier–Stokes equations cast in the Cartesian coordinate system and written in stream function-vorticity form are given as follows:

$$\psi_{xx} + \psi_{yy} = -\omega \tag{1}$$

$$\omega_t + \psi_y\omega_x - \psi_x\omega_y = Re^{-1}(\omega_{xx} + \omega_{yy}) \tag{2}$$

The leading edge of the airfoil is approximated by using a semi-infinite parabola, in a manner similar to work by Werle and Davis[10] and Davis.[11] The results for flow past a parabola compare reasonably well with computational results for the NACA 0012 airfoil[12,13] and may be used to simulate any of the NACA 00XX series with different thicknesses because the leading edges of these airfoils are nearly parabolic in shape. A comparison of the leading edge of the parabola and the NACA 0012 airfoil is shown in Fig. 1. The parabola matches the airfoil leading edge up to approximately 6% of chord. The parabola geometry used here is given by

$$x = \tfrac{1}{2}(y^2 - 1) \tag{3}$$

The frame of reference is attached to the parabola and, therefore, is noninertial. Bhaskaran[12] showed that the additional noninertial terms in the Navier–Stokes equations are negligible compared to other terms if $(\dot{\alpha}l)/V_\infty \ll 1$ holds true, where $\dot{\alpha}$ is the pitch rate. With the cases considered in this study, this parameter is much smaller than one, and so the noninertial terms are ignored.

It is advantageous to cast the governing equations in a parabolic coordinate system (ξ', η') to produce an orthogonal body-fitted grid. The parabolic coordinate system is related to the Cartesian system through the following transformations:

$$x = (\xi'^2 - \eta'^2)/2, \qquad y = \xi'\eta' \tag{4}$$

The stream function and vorticity transport equations (1) and (2) can be transformed using the preceding relations and written as

$$\psi_{\xi'\xi'} + \psi_{\eta'\eta'} = -(\xi'^2 + \eta'^2)\omega \tag{5}$$

$$-(\xi'^2 + \eta'^2)\omega_t + \psi_{\xi'}\omega_{\eta'} - \psi_{\eta'}\omega_{\xi'} + Re^{-1}(\omega_{\xi'\xi'} + \omega_{\eta'\eta'}) = 0 \tag{6}$$

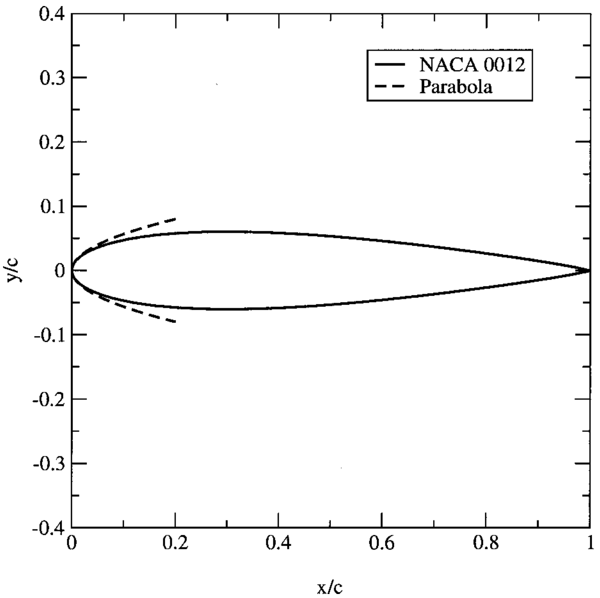

Fig. 1 Comparison of the leading-edge region for the NACA 0012 and the parabola.

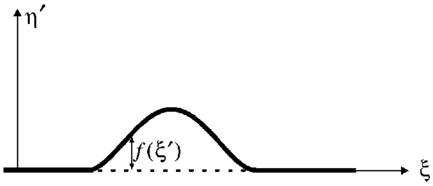

Fig. 2 Schematic diagram of the shearing transformation (or Prandtl transposition).

The surface roughness on the leading edge of the parabola is introduced using a shearing transformation (or Prandtl transposition) similar to work reported by Lynn and Rothmayer.[14] The shearing transformation allows the surface perturbation to be directly embedded within the governing flow equations. Therefore, the algorithm can be applied to a wide range of single-valued roughness geometries with no need for regridding, even when the surface geometry changes. The shearing transformation is shown in Fig. 2 and is given by

$$\xi' = \xi, \qquad \eta' = \eta + f(\xi) \tag{7}$$

where $f(\xi)$ is a known analytic expression. To resolve flow features within localized regions near the leading edge, grid stretching is also applied to the governing equations:

$$\bar{\xi} = \bar{\xi}(\xi), \qquad \bar{\eta} = \bar{\eta}(\eta) \tag{8}$$

The transformation from the uniform-grid computational space to physical space involves multiple steps given by the preceding equations. The overall transformation process is summarized in Fig. 3.

In the study by Bhaskaran and Rothmayer,[15,16] it was found that the convergence rate was improved if the flow variables were split into an inviscid part and a viscous part. When this technique is used, the total stream function ψ and vorticity ω are given by

$$\psi = \Psi + \psi_{\text{inv}}, \qquad \omega = \Omega + \omega_{\text{inv}} \tag{9}$$

where $\omega_{\text{inv}} = 0$ for potential flow. When the transformation equations for the surface roughness and grid generation are used, and the flow variable splitting technique is used Eqs. (5) and (6) can be written in the form

$$\Psi_\tau - \beta^2\Omega = \bar{\xi}_{\xi\xi}\Psi_{\bar{\xi}} + (\bar{\xi}_\xi)^2\Psi_{\bar{\xi}\bar{\xi}} - f_{\xi\xi}\bar{\eta}_\eta\Psi_{\bar{\eta}} - 2f_\xi\bar{\xi}_\xi\bar{\eta}_\eta\Psi_{\bar{\xi}\bar{\eta}}$$
$$+ \left[1 + (f_\xi)^2\right]\bar{\eta}_{\eta\eta}\Psi_{\bar{\eta}} + \left[1 + (f_\xi)^2\right](\bar{\eta}_\eta)^2\Psi_{\bar{\eta}\bar{\eta}} \tag{10}$$

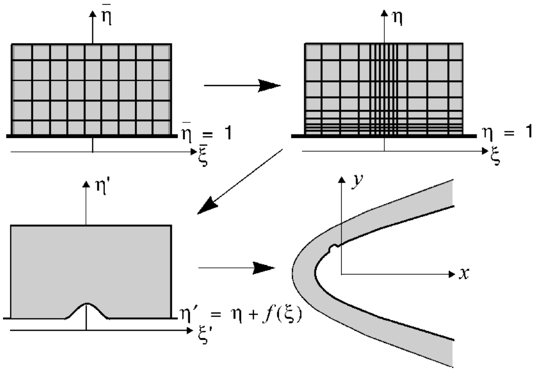

Fig. 3 Schematic diagram of the overall transformation from the computational space to physical space.

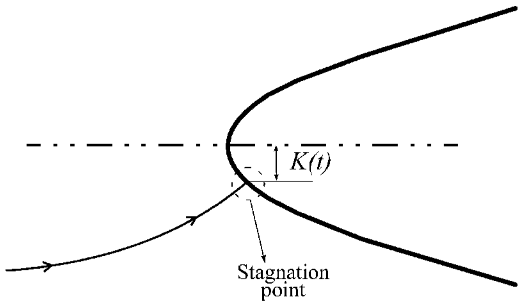

Fig. 4 Schematic diagram of angle of attack parameter $K(t)$.

$$
\begin{aligned}
&\Omega_\tau + \beta^2\Omega_t + \bar{\xi}_\xi\bar{\eta}_\eta(\Psi_{\bar{\eta}}\Omega_{\bar{\xi}} - \Psi_{\bar{\xi}}\Omega_{\bar{\eta}}) \\
&\quad + (\psi_{\text{inv}})_\eta\bar{\xi}_\xi\Omega_{\bar{\xi}} - f_\xi(\psi_{\text{inv}})_\eta\bar{\eta}_\eta\Omega_{\bar{\eta}} - (\psi_{\text{inv}})_\xi\bar{\eta}_\eta\Omega_{\bar{\eta}} \\
&\quad = Re^{-1}\Big\{\bar{\xi}_{\xi\xi}\Omega_{\bar{\xi}} + (\bar{\xi}_\xi)^2\Omega_{\bar{\xi}\bar{\xi}} - f_{\xi\xi}\bar{\eta}_\eta\Omega_{\bar{\eta}} - 2f_\xi\bar{\xi}_\xi\bar{\eta}_\eta\Omega_{\bar{\xi}\bar{\eta}} \\
&\quad + \big[1 + (f_\xi)^2\big]\bar{\eta}_{\eta\eta}\Omega_{\bar{\eta}} + \big[1 + (f_\xi)^2\big](\bar{\eta}_\eta)^2\Omega_{\bar{\eta}\bar{\eta}}\Big\}
\end{aligned}
\tag{11}
$$

where $\beta^2 = \xi^2 + \eta^2 + 2\eta f + f^2$. To help stabilize the method during global iterations, a fictitious time-derivative term (or pseudotime term) is added to both the stream function equation (10) and the vorticity transport equation (11), that is, Ψ_τ and Ω_τ, respectively. At each physical time step, the solution is converged in pseudotime.

Inviscid Flow

There exists an analytic solution for the inviscid potential flow past a parabola from Werle and Davis[10] and Van Dyke.[17] For a clean parabola, the inviscid stream function is given by

$$\psi_{\text{inv}} = [\xi' + K(t)](\eta' - 1) \tag{12}$$

where $K(t)$ is the angle-of-attack parameter, as shown in Fig. 4. $K(t)$ can be related to the angle of attack of the airfoil when the parabolic leading edge is coupled to a thin airfoil description of the full airfoil. In the present study, $K(t)$ is an input parameter that is either constant or a known function of time and can be used to simulate any desired motion of the parabola relative to the freestream, that is, the parabola remains fixed as the stagnation point traverses the leading edge. The particular variation of $K(t)$ used to place the leading edge in pitch up is given by Bhaskaran,[12]

$$K(t) = \frac{\dot{K}_0}{2}\left\{t + \frac{1}{a}\left[\frac{\cosh(at + b)}{\cosh(b)}\right]\right\} \tag{13}$$

$\dot{K}_0$ is the asymptotic value of the final pitch, which is equal to 0.5 in this study. This pitching function corresponds to a leading edge being pitched up at a constant rate, with a smooth transition from the 0-deg angle of attack to the constant pitch rate.

Applying the Prandtl transposition to Eq. (12) produces the inviscid potential solution for the stream function of the parabola with surface roughness present:

$$\psi_{\text{inv}} = [\xi + K(t)][\eta + f(\xi) - 1] \tag{14}$$

Boundary Conditions

No-slip boundary conditions, with $u = v = 0$, are applied at the surface of the parabola ($\eta = 1$). In terms of the stream function, this boundary condition translates to $\psi = 0$ and $\psi_\eta = 0$. When flow-variable splitting is applied, at $\eta = 1$ the no-slip boundary conditions become

$$\Psi = -\psi_{\text{inv}}, \qquad \Psi_{\bar{\eta}} = -[(\psi_{\text{inv}})_\eta / \bar{\eta}_\eta] \tag{15}$$

A second-order accurate one-sided finite difference formulation is used to discretize Eq. (15).

At the far-field boundary, η large but finite, the viscous effects die out and a fully inviscid flow is recovered. Therefore, the split viscous variables Ψ and Ω are assumed to be zero at this boundary. The resulting far-field boundary conditions as $\eta \to \infty$ are

$$\psi = \psi_{\text{inv}}, \qquad \Omega = 0 \tag{16}$$

The viscous solution for flow past a parabola is known to approach the Blasius solution as $\xi \to \infty$ (see Ref. 11). As $\xi \to \infty$, then ψ and ω are given by the following:

$$\psi \sim \xi g(\eta), \qquad \omega \sim -[h(\eta)/\xi] \tag{17}$$

Therefore, at the far-downstream boundary, the flow is assumed to be steady and the preceding expressions for the Blasius solution are used to evaluate the streamwise derivatives, as

$$\psi_\xi \sim \psi/\xi, \qquad \psi_{\xi\xi} \sim 0 \tag{18}$$

$$\omega_\xi \sim -(\omega/\xi), \qquad \omega_{\xi\xi} \sim 2\omega/\xi^2 \tag{19}$$

The upper and lower downstream boundaries are placed at a large but finite value of $|\xi|$.

Numerical Method

An implicit numerical method is used to solve Eqs. (10) and (11). The numerical scheme is second-order accurate in time and space, with central differences used for the spatial derivatives and a backward difference for the temporal derivative. The nonlinear convective terms are linearized using Newton linearization and mixed derivatives are treated iteratively as source terms.

As a starting solution for the full Navier–Stokes algorithm, the parabolized Navier–Stokes equations are solved for flow past a parabola at a constant angle of attack, and the solution is used as input to start the full Navier–Stokes calculations. The parabolized Navier–Stokes solver uses the Blasius solution as a starting solution.

The implicit scheme sweeps in both the ξ and η directions, with the sweeps in the ξ direction being bidirectional and the sweeps in η being unidirectional. One complete spatial sweep consists of two alternating sweeps in the streamwise direction, ξ, and one sweep in the normal direction, η, which is equivalent to one pseudotime step. Each sweep involves the solution of a 2×2 block-tridiagonal system of equations.

For unsteady flow, the code marches the solution in time and, at each physical time step, the pseudotime terms are iterated to convergence before moving to the next physical time step. The algorithm has the capability of solving for purely steady flow by either 1) allowing the unsteady code to eventually converge to a steady solution or 2) eliminating the time term Ω_t and solving the remaining steady Navier–Stokes equations. With this particular algorithm, if the flowfield is truly steady, then either method can be used to obtain the solution. If the flow is unsteady, then the "steady" flow solver may not converge.

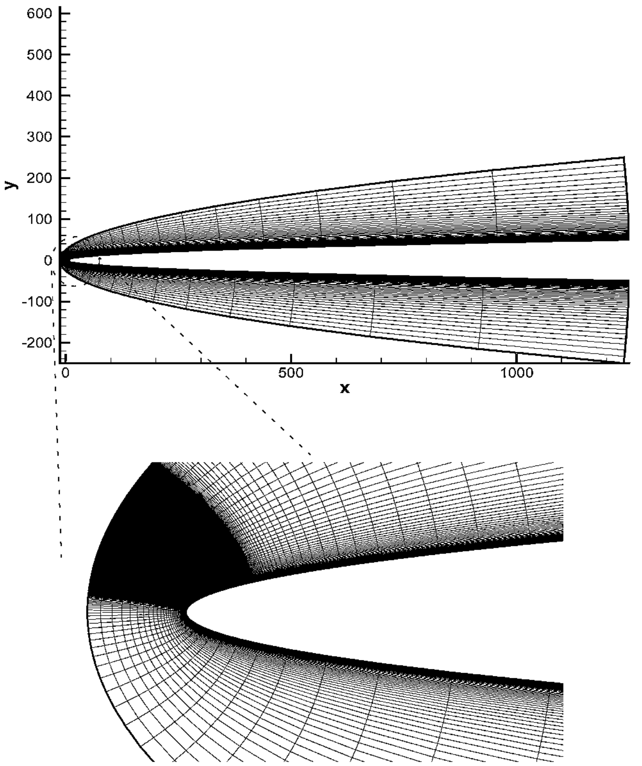

Fig. 5 Typical grid used for the dynamic-stall computations (481 × 81) with 380 streamwise grid points in the dense-grid region.

The grid used for the computations is a structured, body-fitted grid. A region of dense, uniformly spaced grid points in the streamwise direction is placed in the vicinity of the parabola leading edge, with hyperbolic stretching upstream and downstream of this region. Stretching is also used in the normal direction to cluster points near the surface. A typical parabolic grid is shown in Fig. 5. The grid in this figure is 481 × 81, with 380 streamwise grid points placed in the dense-grid region near the leading edge. In Fig. 5, the leading edge of the parabola has a clean surface. When roughness is present, typically the grid requirements are increased to resolve the flow about each roughness element. In this study, the grids ranged from 481 × 81 to 1501 × 201. In general, the flow solution was more sensitive to the grid density in the streamwise direction than in the normal direction when surface roughness was present.

Surface Protuberance

The surface protuberance (or roughness) is added to the baseline parabolic surface using a Prandtl transposition, which allows new surface-oriented coordinates to be easily generated without the need for regridding. For example, alterations to the surface roughness geometry can be made without changing the actual grid parameters.

The current work uses an analytic roughness geometry for the surface protuberance. This produces a smooth hump with variable height and wavelength. The hump equation used is given as

$$f(\xi) = h(\xi - \xi_L)^5(\xi_R - \xi)^5 \tag{20}$$

A 10th-order polynomial was used to ensure a smooth transition from the roughness element to the parabola surface. This helped to alleviate any curvature discontinuity problems at the juncture point.

Both simple and complex analytic hump geometries are used to simulate different types of leading-edge roughnesses. The simple roughness is either a single smooth hump placed on the parabola leading edge or multiple humps with equal height and wavelength arranged to simulate distributed roughness. The complex roughness is created by superimposing multiple humps of varying heights and wavelengths to produce a more geometrically complex roughness shape. Figure 6 shows one of the complex roughness geometries that was evaluated in this study. The roughness in Fig. 7 is also a complex roughness shape, but was selected to more closely match a leading-edge glaze-ice roughness shape.

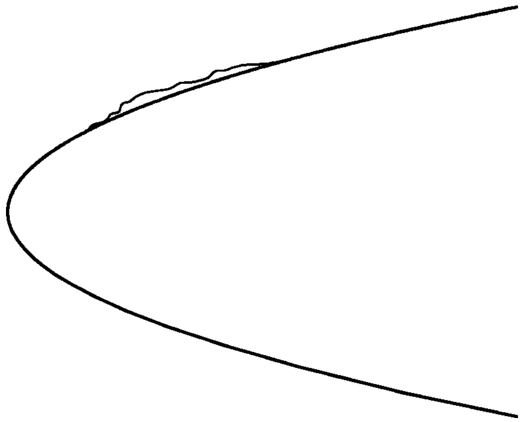

Fig. 6 Complex leading-edge roughness formed by superimposing multiple roughness elements of varying height and wavelength.

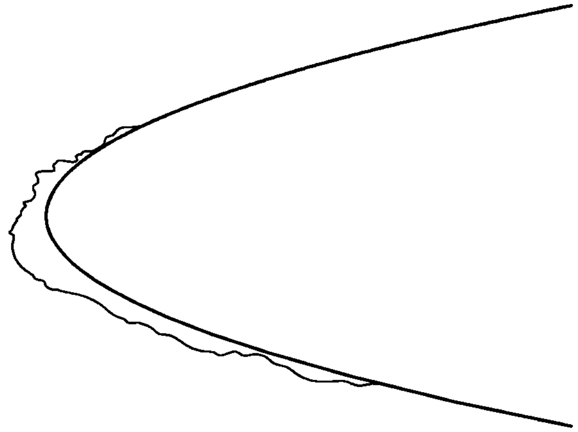

Fig. 7 Simulated leading-edge ice shape representing a short accretion time.

Reynolds Number Scaling

In the present work, the parabola Reynolds number Re_l can be related to the airfoil chord Reynolds number Re_c by

$$Re_l = (l/c)Re_c \tag{21}$$

For the NACA 0012 airfoil, the (l/c) ratio is equal to 0.016 (Abbott and Von Doenhoff[18]). This allows computation of the leading-edge flowfield at a significantly lower Reynolds number Re_l than that of the chord Reynolds number (approximately two orders of magnitude). For the majority of cases presented here, Re_l varied from 159 to 1×10^4. For the NACA 0012 airfoil, the corresponding Re_c ranges from 1×10^4 to 6.3×10^5.

Flow Separation and Dynamic-Stall Results

The impact of surface roughness on flow separation and dynamic stall is investigated, including simple roughness and complex roughness shapes. The algorithm is capable of producing results for both steady flow at a constant angle of attack [$K(t)$ value] and unsteady flow at a constant angle of attack or in pitch up. The rapid pitch up of the leading edge produces the dynamic-stall phenomenon. Results are presented for steady and unsteady flow for clean and roughened surfaces.

Clean Airfoil

Preliminary work was done with the current algorithm to verify the validity of the results. Comparisons were made to existing experimental and computational work for steady and unsteady flow past a clean airfoil, including dynamic-stall comparisons.

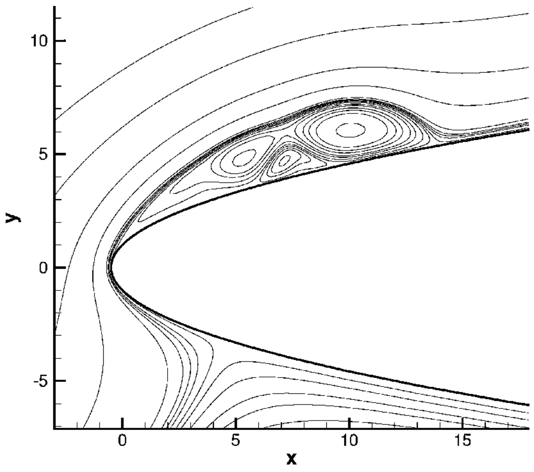

Current simulation

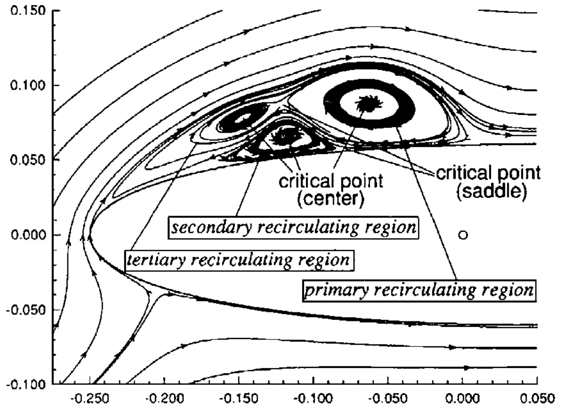

Benchmark case

Fig. 8 Comparison of streamline patterns for pitch-up case.

One of the benchmarks for prediction of the dynamic-stall process was comparing results to the work done by Choudhuri et al.[7] Their computations are based on the two-dimensional compressible Navier–Stokes equations for the NACA 0012 at $Re_c = 1 \times 10^4$. Their work used two separate algorithms (structured and unstructured grid) to perform the calculations, and the results were in good agreement. The dynamic stall is initiated by a constant rate pitch-up maneuver. The pitch rate equation used in the present study was altered to match that of Ref. 7. The case chosen for comparison is the dynamic-stall results at $\alpha = 22.5$ deg. For the present work, the following parameters were used to match the flow conditions: $Re_l = 159$ ($Re_c = 1 \times 10^4$) and $K = 3.2$. Bhaskaran[12] showed that setting the angle-of-attack parameter to $K = 3.2$ for the parabola was equivalent to $\alpha = 22.5$ deg.

The results of this comparison are shown in Fig. 8, which is a plot of the stream function contours. We see that there is close correspondence between the two results. Both of the computational results show the same three distinct recirculation regions at this point in the pitch up. The shapes and relative locations of the primary, secondary, and tertiary recirculating regions compare well between the two results. Mutual interaction between the primary and secondary eddies eventually leads to the shedding of vorticity from the wall and subsequent convection downstream. The differences between the two plots can most likely be attributed to the geometry differences between the NACA 0012 and the parabola leading edge; the parabola only matches the NACA 0012 to approximately 6% of chord, whereas the recirculating regions in these plots spread out to approximately 30% of chord. Suito and Ishii[9] also obtained similar results that are in good agreement with the current results.

The second test case is a comparison to a parabola in pitch up from the computational work done by Bhaskaran and Rothmayer.[15,16] The results are based on $Re_l = 1 \times 10^3$ for a clean parabola leading-edge region. The simulations from the present work are in excellent agreement with these results throughout the pitch up and formation of the dynamic-stall vortex.

A majority of the work for the clean leading edge was completed with a 481 × 81 grid. The dense-grid region on the upper surface contained 380 streamwise grid points. Ghia et al.[19] found that a C grid of 444 × 101 for the entire airfoil was sufficient to resolve the dominant scales of the dynamic-stall problem. Therefore, it was assumed that the dense-grid region placed on the leading edge would be more than adequate to resolve the flowfield. However, a grid study was performed to ensure a grid-independent solution.

Figure 9 shows the results of this grid-dependence study. The grid was refined in both the streamwise and normal directions from 481 × 81 to 881 × 101. In Fig. 9, wall vorticity Ω_w was used to demonstrate a grid-independent solution. Note that $-\Omega_w$ is proportional to the wall shear stress. Figure 9 shows that the two solutions are in good agreement.

Simple Roughness

Several different cases were run with the simple roughness geometries on the leading edge of the parabola. The first case to be investigated was a single smooth hump on the upper leading-edge surface, with the hump being fully contained within the boundary layer. The hump height is approximately one-third of the approaching laminar boundary-layer height. A stream function contour plot is shown in Fig. 10. This particular case was at a constant angle of

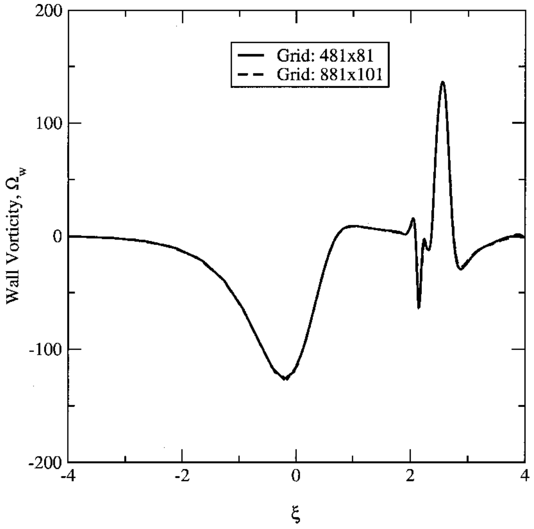

Fig. 9 Grid-dependence study for an unsteady flow showing wall vorticity on upper surface of a clean leading edge during formation of dynamic-stall vortex at $t = 32$.

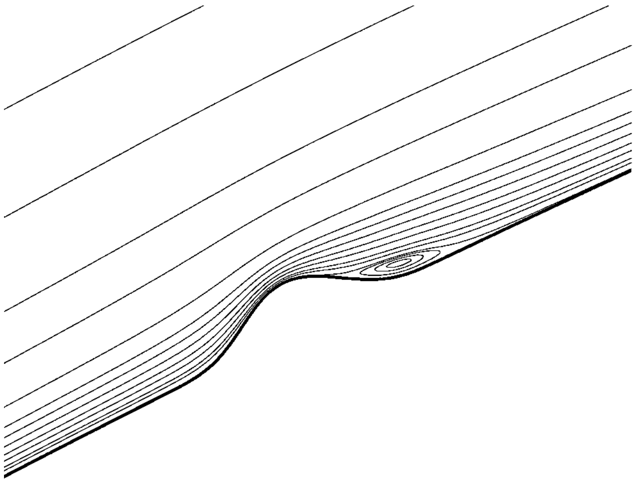

Fig. 10 Flow past a single analytic hump placed on the leading edge showing a steady laminar separation bubble, $Re_l = 1 \times 10^3$.

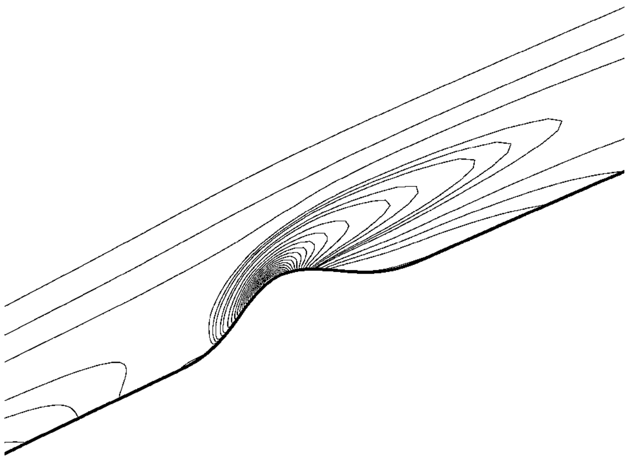

Fig. 11 Vorticity contours for flow past a single analytic hump.

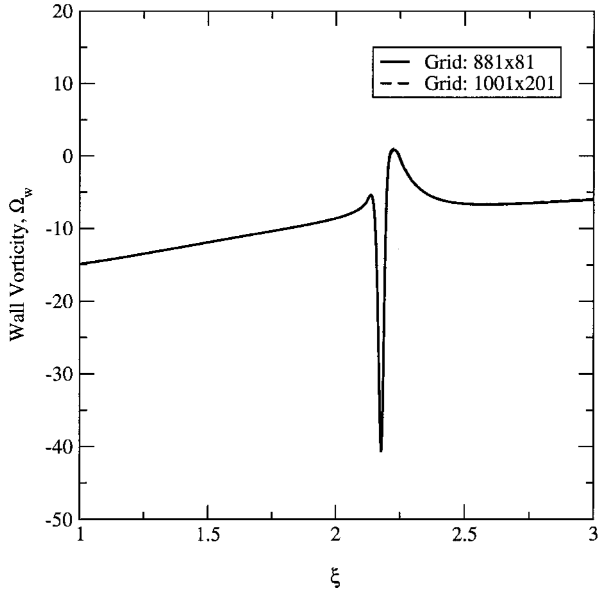

Fig. 12 Grid-dependence study for flow past a single hump on the leading edge, shown in Fig. 10.

attack of $K = 0.0$ (0-deg angle of attack), $Re_l = 1 \times 10^6$, and a grid of 881×81, with the dense-grid boundaries placed upstream and downstream of the hump. Both the steady and unsteady flow solvers were applied to this case, and both produced identical results. The unsteady flow solver converged to a steady solution. As Fig. 10 shows, the hump geometry produced a steady, laminar separation bubble on the downstream side of the hump. Vorticity contours have also been plotted for this case and are shown in Fig. 11. Qualitatively, Fig. 11 is consistent with results for flow past a hump on a flat plate, such as in the work done by Kiya and Arie[20] and Haussling.[21]

Grid independence of the flow solution was periodically checked throughout the course of this work. For the single leading-edge roughness element, results for the grid-independence test are presented in Fig. 12, which shows that the grid resolution used in this case is sufficient to capture the flow past the isolated hump. For a grid-independent solution, the required grid resolution is approximately 40–50 streamwise grid points for an individual hump.

As expected, the evaluation of grid dependence in this work revealed that the more complex geometries require a finer grid to resolve the flow physics correctly. As mentioned earlier, once roughness has been added to the surface, the grid is more sensitive to the number of streamwise grid points than the normal grid points. This assumes that you already have an adequate number of grid points in the normal direction to resolve the flow past a clean surface.

A second case of simple roughness was tested, which consisted of eight simple humps placed on the upper-surface leading edge to simulate distributed roughness. The flow conditions were the same as for the single-hump case: a constant angle of attack of $K = 0.0$ and $Re_l = 1 \times 10^3$. The unsteady flow solver converged to a steady-state solution for this roughness geometry. As in the single-hump case, the distributed roughness was fully contained within the boundary layer. The dense-grid region was fine enough to capture the small-scale separation regions contained between the roughness elements. Figure 13 shows the stream function contour plot for this case. It also includes a closeup showing the local separation between the roughness elements. This case produced steady, laminar flow separation for the given Reynolds number Re_l.

This particular roughness geometry was also used in an unsteady pitch-up case. The simulation was run out in time until a full dynamic-stall vortex was formed and vortex structures began

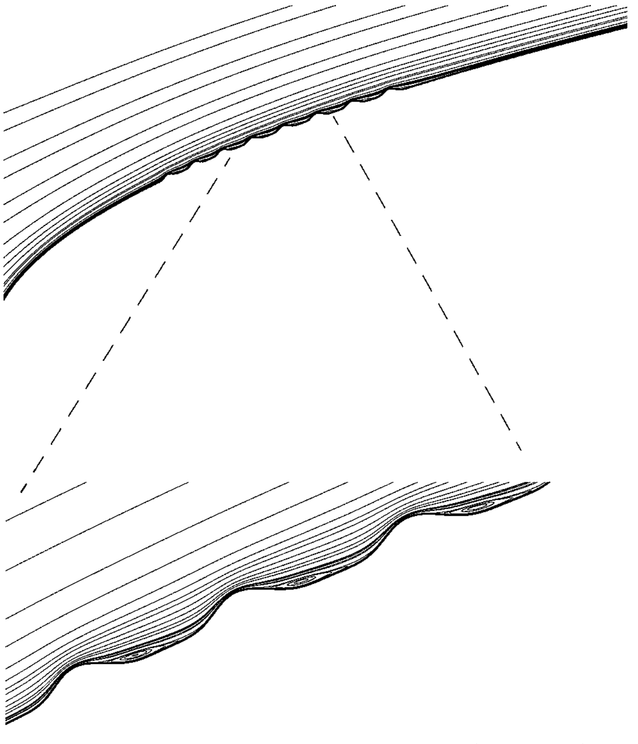

Fig. 13 Stream function plot for simple roughness (eight hump) with steady, laminar flow at 0-deg angle of attack, $Re_l = 1 \times 10^3$.

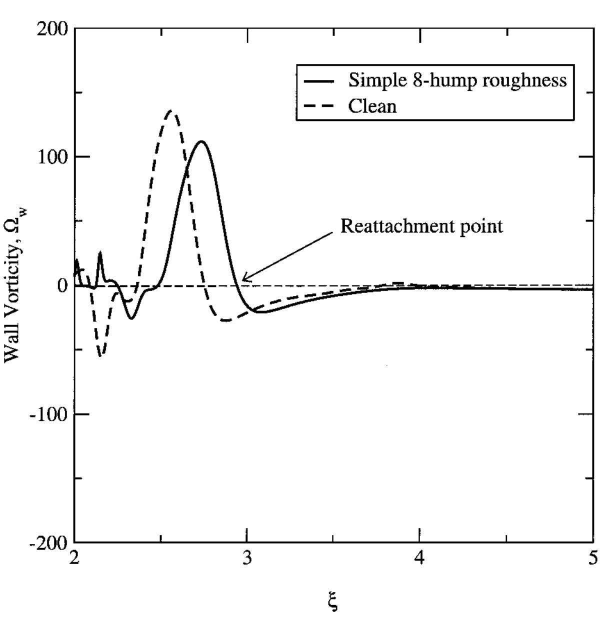

Fig. 14 Comparison of wall vorticity during pitch-up at $t = 32$, $Re_l = 1 \times 10^3$.

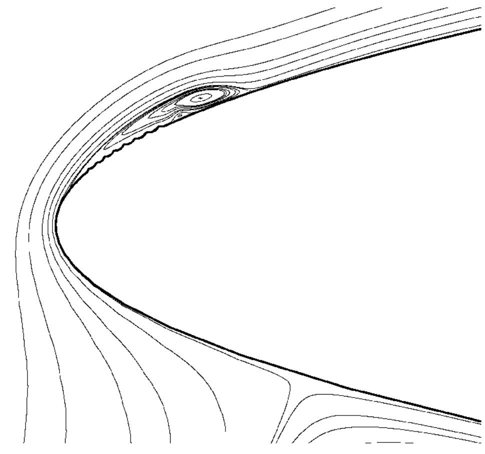

Simple eight-hump roughness

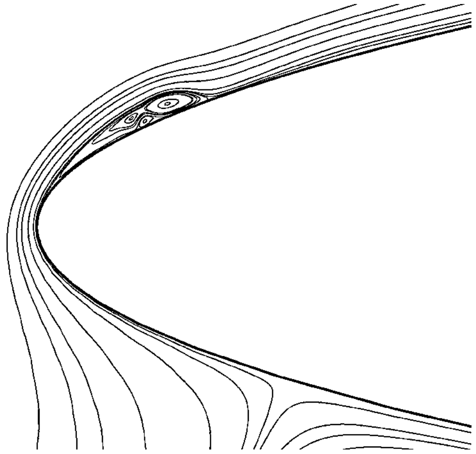

Clean

Fig. 15 Comparison of dynamic-stall characteristics at the airfoil leading edge during pitch up at $t = 32$ and $Re_l = 1 \times 10^3$ (stream function contour plot).

shedding from the surface. Comparing the results during pitch up to the clean airfoil case, there is no significant differences for much of the initial dynamic-stall sequence. It appears that the dynamic-stall phenomenon is robust enough to swallow any small-scale perturbations to the flow produced by this roughness in the early stages of pitch up. However, after the formation of the primary vortex near the leading edge, some differences become apparent.

Figure 14 shows the wall vorticity for the clean and eight-hump roughness cases at a physical time of $t = 32$ ($K = 3.25$) during pitch up. This plot shows that the dynamic stall vortex system for the eight-hump roughness case reattaches farther downstream than for the clean case. Both have the same upstream separation point (not shown in Fig. 14). This can also be seen in Fig. 15, which is a plot of the stream function contours for both the eight-hump roughness geometry and the clean surface.

Figure 15 also shows another item of interest: The small-scale roughness modifies the secondary separation mechanism in the dynamic stall. The eight-hump roughness case shows that the primary vortex has been formed and that there exists the beginning of a secondary recirculating region. However, for the clean case (at the same physical time), the formation of a primary, secondary, and a tertiary vortex (or a second primary vortex) is already complete. The interaction between the first and second primary vortices is what induces the first primary vortex to be shed from the surface. The vorticity contours for the distributed roughness case at $t = 32$ are shown in Fig. 16. In this stage of pitch up, the vorticity is being rolled up to form a vortex, which induces the secondary separation region.

Complex Roughness

Two complex roughness geometries were also investigated in this work under dynamic-stall conditions. For the first geometry, Fig. 17 shows a stream function comparison between leading edges with and without surface roughness. Both airfoils are at the same physical time station, $t = 30$, in the pitch up and have the same Reynolds number Re_l, with the only difference being the implementation of the surface roughness. For this roughness geometry, the height is larger than the approaching boundary-layer thickness.

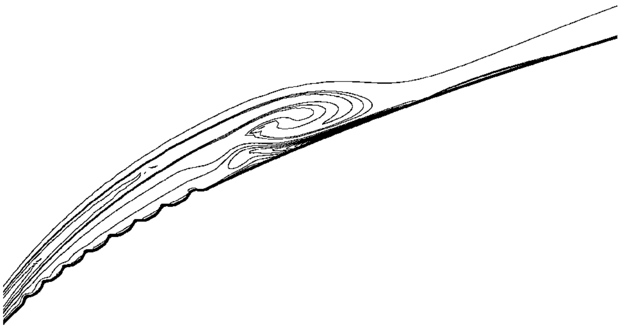

Fig. 16 Vorticity contours in the region of the simple eight-hump roughness during pitch up of the leading edge at $t = 32$, $Re_l = 1 \times 10^3$.

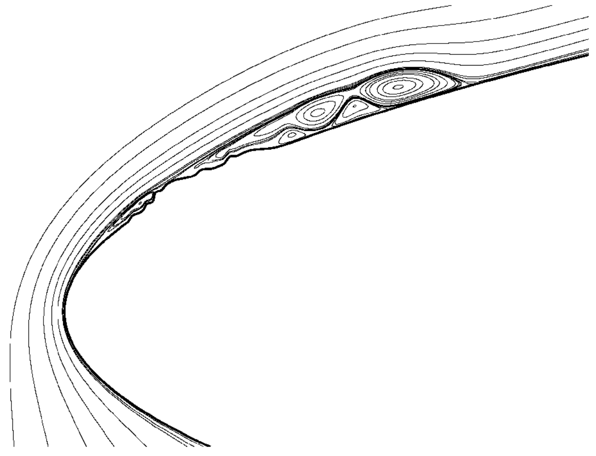

Complex roughness

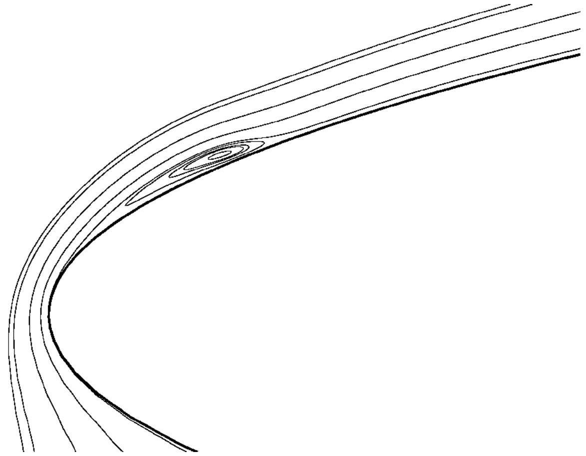

Clean

Fig. 17 Comparison of dynamic-stall characteristics stream function contour plot at the airfoil leading edge for $Re_l = 1 \times 10^3$ and $t = 30$.

Figure 17 clearly shows the leading-edge roughness significantly alters the inception time for the formation of the dynamic-stall vortex. At this temporal station, the clean airfoil is just beginning to show a thin recirculating bubble on the upper leading edge. However, the airfoil with roughness has already migrated to a more advanced stage of the dynamic stall. There are multiple primary and secondary vortices interacting in the leading-edge region. Eventually, this interaction of the first primary vortex and the first secondary vortex will lead to the vortex being shed from the surface and convected downstream.

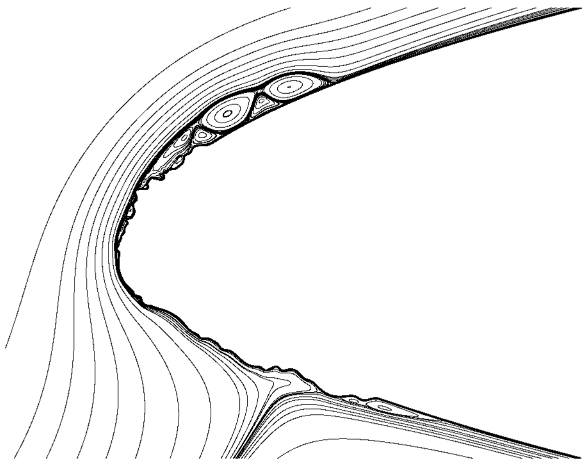

Simulated ice roughness

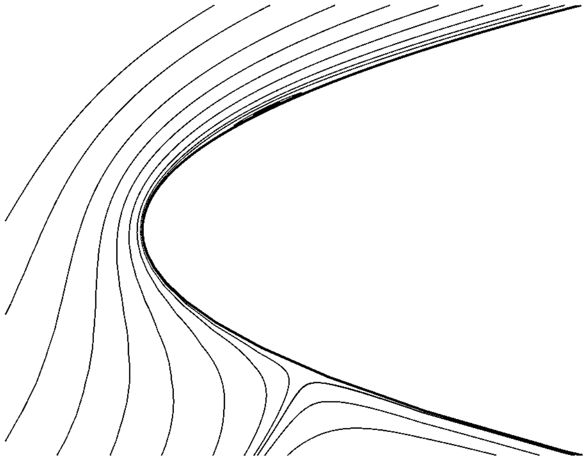

Clean

Fig. 18 Comparison of dynamic-stall characteristics stream function contour plot at the airfoil leading edge for $Re_l = 1 \times 10^3$ and $t = 24$.

The other complex roughness geometry is fashioned to simulate a leading-edge ice shape (Fig. 7). Similar to the preceding complex roughness shape, a comparison is made to the results for a clean parabola at the same time during pitch up. The results of this comparison are shown in Fig. 18 for $Re_l = 1 \times 10^3$ and at $t = 24$ in the pitch-up sequence. This roughness geometry produces an even more pronounced effect on the dynamic-stall vortex than the earlier geometry, with a dramatic difference in the flowfield on the leading edges. The parabola with the simulated ice roughness is at the stage just before vortex shedding even at the early time of $t = 24$, whereas the clean case is just beginning the formation a thin recirculating bubble on the leading edge. Obviously, the larger, more complex ice shape can have a significant impact on the formation of the dynamic-stall vortex. The stream function contours clearly show the formation of primary, secondary, and tertiary separation regions. At this physical time, the primary and secondary vortices on the upper surface are at a level similar to those seen for the first complex roughness geometry at a physical time of $t = 30$ (both at the same Reynolds number). Therefore, the simulated ice shape triggers the dynamic stall at an earlier stage than the previous complex roughness shape.

Plots of the instantaneous vorticity contours at various times during the pitch-up maneuver are shown in Fig. 19 for the leading edge with the simulated ice shape. These vorticity contour plots detail the evolution of the dynamic-stall vortex with the primary vortex eventually being shed from the surface. At $t = 16.0$, a shear layer is present with a vortex forming downstream of the roughness. This vortex strengthens and induces a secondary separation region. The mutual interaction of the primary and secondary vortices causes the vortex to be shed from the wall and convected downstream, which can be seen at $t = 31.5$.

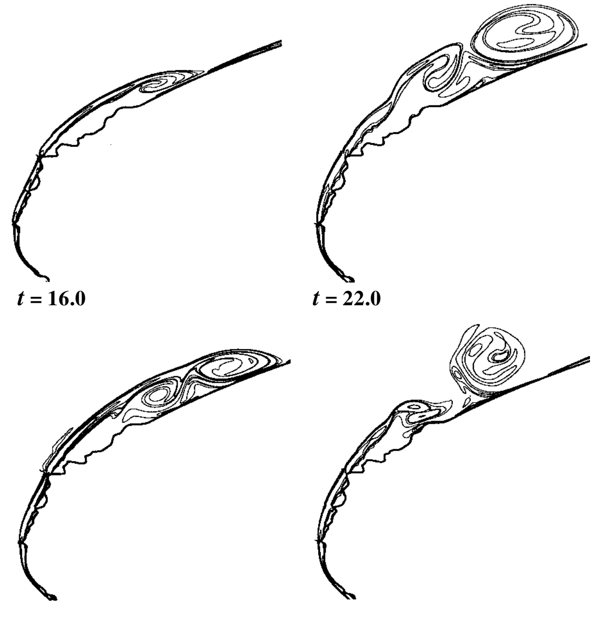

$t = 16.0$ $t = 22.0$

$t = 29.0$ $t = 31.5$

Fig. 19 Various temporal snapshots of the vorticity contours for the simulated ice roughness case under dynamic-stall flow conditions.

Reynolds number effects were also investigated for the simulated ice shape. The Reynolds number based on leading-edge radius of curvature was increased from 1×10^3 to 1×10^4 (The corresponding chord Reynolds number $Re_c \rightarrow 6.3 \times 10^4$ to 6.3×10^5.) As before, the parabola was set into motion with a constant-rate pitch up to simulate the dynamic-stall phenomenon. The increase in Reynolds number Re causes the flow in the leading-edge region to become highly unsteady even in the early stages of pitch up. For the cases at $Re_l = 1 \times 10^3$, the separation regions remained steady and laminar for a longer time into the pitch up.

Summary

In this study, the impact of surface roughness on unsteady flow past an airfoil leading edge is investigated using a two-dimensional Navier–Stokes algorithm. Solutions are obtained for both steady and unsteady flow at constant angle of attack and in pitch up with surface roughness present on the leading edge. The key findings of this study are summarized as follows.

1) It was shown that this type of leading-edge analysis can be used as an efficient tool to investigate flow separation and local-stall characteristics in the leading-edge region of an airfoil.

2) The implementation of the Prandtl transposition within the governing equations allows the algorithm the flexibility of easily incorporating many different roughness geometries (simple to complex) for analysis.

3) Small-scale surface roughness (smaller than the boundary-layer height) affects the secondary separation mechanism in dynamic stall.

4) Large-scale roughness can significantly alter the inception time for the formation of the dynamic-stall vortex.

Acknowledgments

This work was supported through a NASA Graduate Student Research Fellowship under Contract NGT3-52332 by the Icing Branch at the NASA John H. Glenn Research Center at Lewis Field. The Technical Advisor for this fellowship is Mark Potapczuk and the authors would like to thank him for his help and guidance on this work.

References

[1] Potapczuk, M. G., Bragg, M. B., Kwon, O. J., and Sankar, L. N., "Simulation of Iced Wing Aerodynamics," NASA TM-104362, 1991.

[2]Cebeci, T., "Effects of Environmentally Imposed Roughness on Airfoil Performance," NASA CR-179639, 1987.

[3]Cebeci, T., and Besnard, E., "Prediction of the Performance Degradation of an Aircraft in Natural Icing Conditions," AIAA Paper 94-0487, Jan. 1994.

[4]Shih, C., Lourenco, L. M., and Krothapalli, A., "Investigation of Flow at Leading and Trailing Edges of Pitching-Up Airfoil," *AIAA Journal*, Vol. 33, No. 8, 1995, pp. 1369–1376.

[5]Carr, L., "Progress in Analysis and Prediction of Dynamic Stall," *Journal of Aircraft*, Vol. 25, No. 1, 1988, pp. 6–17.

[6]Carr, L., and McCroskey, W. J., "A Review of Recent Advances in Computational and Experimental Analysis of Dynamic Stall," *International Union of Theoretical and Applied Mechanics Symposium on Fluid Dynamics at High Angle of Attack*, Tokyo, Japan, Sept. 1992.

[7]Choudhuri, P. G., Knight, D. D., and Visbal, M. R., "Two-Dimensional Unsteady Leading-Edge Separation on a Pitching Airfoil," *AIAA Journal*, Vol. 32, No. 4, 1994, pp. 673–681.

[8]Robinson, M., Helin, H., Gilliam, F., Russell, J., and Walker, J., "Visualization of Three-Dimensional Forced Unsteady Separated Flow," AIAA Paper 86-1066, 1986.

[9]Suito, H., and Ishii, K., "Simulation of Dynamic Stall by Multi-Directional Finite-Difference Method," AIAA Paper 95-2264, June 1995.

[10]Werle, M. J., and Davis, R. T., "Incompressible Laminar Boundary Layers on a Parabola at Angle of Attack: A Study of the Separation Point," *Journal of Applied Mechanics*, American Society of Mechanical Engineers, Paper 71-APM-31, 1971.

[11]Davis, R. T., "Numerical Solution of the Navier–Stokes Equations for Symmetric Laminar Incompressible Flow Past a Parabola," *Journal of Fluid Mechanics*, Vol. 51, No. 3, 1972, pp. 417–433.

[12]Bhaskaran, R., "Unsteady Viscous Flow Past Stationary, Pitching or Oscillating Airfoil Leading Edges," Ph.D. Dissertation, Dept. of Aerospace Engineering and Engineering Mechanics, Iowa State Univ., Ames, IA, 1996.

[13]Reisenthal, P. H., and Childs, R. E., "A Study of Reynolds Number Effects on Incipient Leading Edge Stall," AIAA Paper 94-2339, 1994.

[14]Lynn, J., and Rothmayer, A. P., "Viscous Flows Past Short-Scaled Humps and Surface Blowing," *European Journal of Mechanics-B/Fluids*, Vol. 12, No. 3, 1993, pp. 313–321.

[15]Bhaskaran, R., and Rothmayer, A. P., "Validation of a Navier–Stokes Solver for the Leading-Edge Flow Past Pitching and Oscillating Airfoils," *Proceedings of the 6th International Conference on Computational Fluid Dynamics*, Sept. 1995.

[16]Bhaskaran, R., and Rothmayer, A. P., "Separation and Instabilities in the Viscous Flow Past Airfoil Leading Edges," *Computers and Fluids*, Vol. 27, No. 8, 1998, pp. 903–921.

[17]Van Dyke, M. D., "Second-Order Subsonic Airfoil Theory Including Edge Effects," NASA TR 1274, 1956.

[18]Abbott, I. H., and Von Doenhoff, A. E., *Theory of Wing Sections*, Dover, New York, 1959, p. 321.

[19]Ghia, K. N., Yang, J., Osswald, G. A., and Ghia, U., "Study of Role of Unsteady Separation in Formation of Dynamic Stall Vortex," AIAA Paper 92-0196, 1992.

[20]Kiya, M., and Arie, M., "Viscous Shear Flow Past Small Bluff Bodies Attached to a Plane Wall," *Journal of Fluid Mechanics*, Vol. 69, No. 4, 1975, pp. 803–823.

[21]Haussling, H. J., "Viscous Flows of Stably Stratified Fluids Over Barriers," *Journal of the Atmospheric Sciences*, Vol. 34, No. 4, 1977, pp. 589–602.